Evaluation of additional confinement for three-dimensional geoinclusions under general stress state

Piyush Punetha[1], Sanjay Nimbalkar[2✉] and Hadi Khabbaz[3]

[1]Ph.D. Candidate, School of Civil and Environmental Engineering, FEIT, University of Technology Sydney, NSW 2007, Australia. Email: Piyush.Punetha@student.uts.edu.au, ORCID: 0000-0002-0812-4708.

[2]Lecturer, School of Civil and Environmental Engineering, FEIT, University of Technology Sydney, NSW 2007, Australia. Email: Sanjay.Nimbalkar@uts.edu.au, ORCID: 0000-0002-1538-3396.

[3]Associate Professor, School of Civil and Environmental Engineering, FEIT, University of Technology Sydney, NSW 2007, Australia. Email: Hadi.Khabbaz@uts.edu.au, ORCID: 0000-0001-6637-4601.

✉Corresponding Author: Sanjay Nimbalkar (School of Civil and Environmental Engineering, FEIT, University of Technology Sydney, NSW 2007, Australia. Phone no.: +61 2 95141819. Email: Sanjay.Nimbalkar@uts.edu.au)

ABSTRACT

The three-dimensional cellular geoinclusions (e.g. geocells, scrap tires) offer all-around confinement to the granular infill materials, which improves their strength and stiffness. The accurate evaluation of extra confinement offered by these geoinclusions is inevitable for predicting their performance in the field. The existing models to evaluate the additional confinement are based on either plane-strain or axisymmetric stress states. However, these geoinclusions are more likely to be subjected to the three-dimensional stresses in actual practice. This note proposes a semi-empirical model to evaluate the additional confinement provided by cellular geoinclusions under the three-dimensional stress state. The proposed model is successfully validated against the experimental data. A parametric study is conducted to investigate the influence of input parameters on additional confinement. The results reveal that the simplification of the three-dimensional stress state into axisymmetric or plane-strain condition has resulted in inaccurate and unreliable results. The extra confinement offered by the geoinclusion show substantial variation along the intermediate and minor principal stress directions depending on the intermediate principal stress, infill soil and geoinclusion properties. The magnitude of additional confinement increases with an increase in the geoinclusion modulus. The findings are crucial for the accurate assessment of the in-situ performance of three-dimensional cellular geoinclusions.

Keywords: Cellular geoinclusions; Additional confinement; Mathematical model; General stress state.

INTRODUCTION

The lateral spreading of unbound granular materials (UGM) under train-induced loading poses a severe challenge to the stability of the ballasted railway tracks (Selig and Waters 1994). This lateral movement is often associated with insufficient confinement of UGM layers overlying stiff subgrade soils (Sun et al. 2018; Nimbalkar et al. 2019). Fig. 1(a) shows the loss in track geometry due to the lateral spreading of UGM under the train traffic-induced loads. The three-dimensional (3D) cellular geoinclusions such as geocells, scrap rubber tires, etc. can be employed in the ballasted railway tracks to provide additional confinement and consequently, improve the track stability. As shown in Fig. 1(b), these cellular geoinclusions surround the UGM and create a stiff structure which resists the lateral spreading of UGM (Koerner 2012). Consequently, the loss in track geometry can be minimized.

The 3D cellular geoinclusions are increasingly being used to improve the mechanical properties of granular infill materials. These geoinclusions provide all-around confinement to the infill soil and consequently, prevent its lateral spreading under loads (Zhou and Wen 2008, Leshchinsky and Ling 2013a). The investigations in the past have demonstrated the beneficial role of geocells (e.g., Raymond 2001; Satyal et al. 2018) and scrap tires (e.g. Forsyth and Egan 1976; Garga and O'shaughnessy 2000; Indraratna et al. 2017) in improving the stability of railway tracks and embankments. However, the lack of a well-established method to evaluate the magnitude of additional confinement provided by these geoinclusions has limited their application in the railway tracks.

An insight into the load transfer mechanism, quantification of the benefits and the full-scale performance data is inevitable to develop the design methods for cellular geoinclusions in railway applications. Although experimental and field studies are reliable techniques to gain insight into the behavior of 3D cellular geoinclusions, these investigations require a considerable amount of time and efforts. On the other hand, the analytical and numerical simulations offer cost-effective alternatives to study and predict the response of the cellular geoinclusion reinforced soil. Therefore, researchers have conducted two-dimensional (e.g. Bathurst and Knight 1998) and three-dimensional numerical analysis (e.g. Han et al. 2008; Leshchinsky and Ling 2013a, 2013b; Liu et al. 2018) on geoinclusion-reinforced soil and have reported that the geoinclusions significantly improve the strength and stiffness of the infill soil. However, the magnitude of improvement/ modification depends on the stress state, properties of the infill and the geoinclusions (Nimbalkar et al. 2019).

Several researchers have attempted to evaluate the extra confinement offered by the cellular geoinclusions under static (Bathurst and Rajagopal 1993; Rajagopal et al. 1999) and cyclic/repeated loading conditions (Yang and Han 2013; Indraratna et al. 2015). These models are applicable to two-dimensional (2D) (plane-strain or axisymmetric) stress state. However, the cellular geoinclusions are more likely to be subjected to general stress state (3D) in a real track (e.g., at turnouts, intersections). Therefore, the additional confinement provided by the cellular geoinclusions under general stress state may significantly differ from the plane-strain or triaxial (axisymmetric) stress state.

The present paper describes the theoretical development of a semi-empirical model for evaluating the additional confinement provided by cellular geoinclusions under the 3D stress state. A parametric study is conducted to investigate the influence of infill soil properties, geoinclusion type and stress levels on additional confinement. Moreover, the proposed model is validated against the experimental data available in the literature. The present study is inevitable for assessing the performance of cellular geoinclusion-stabilized infills under the 3D stress state resembling actual track environment.

DEVELOPMENT OF MODEL

General loading condition

When the cellular geoinclusion-reinforced UGM is loaded vertically, the infill material deforms in vertical and lateral directions. The geoinclusion resists the lateral deformation of the infill material, which generate circumferential stresses (tension) along its periphery. These circumferential stresses provide additional confinement to the infill. The magnitude of additional confinement can be evaluated using the hoop tension theory as:

(1a) $$\Delta\sigma_2' = \frac{2\sigma_{c,2}\cdot t_g}{D_g}$$

(1b) $$\Delta\sigma_3' = \frac{2\sigma_{c,3}\cdot t_g}{D_g}$$

where $\Delta\sigma'_2$ and $\Delta\sigma'_3$ are the additional confining pressures in the direction of intermediate (σ'_2) and minor principal stresses (σ'_3), respectively; $\sigma_{c,2}$ and $\sigma_{c,3}$ are the circumferential stresses in the direction of σ'_2 and σ'_3, respectively; D_g and t_g are diameter and thickness of geoinclusion, respectively. The derivation of Eqs. (1a) and (1b) is given in Appendix.

The circumferential stress is determined using the Hooke's law (Timoshenko and Goodier, 1970)

(2) $$\sigma_c = \frac{M_m}{t_g}\left[\frac{(1-\mu_g)\varepsilon_c + \mu_g\varepsilon_r}{(1+\mu_g)(1-2\mu_g)}\right]$$

where M_m is the mobilized modulus of geoinclusion per unit width; μ_g is the Poisson's ratio of geoinclusion; ε_c and ε_r are circumferential and radial strains in the geoinclusion, respectively.

Figs. 2a–2c show the deformation profiles of the cellular geoinclusions for general ($\sigma'_1 \neq \sigma'_2 \neq \sigma'_3$ and $\varepsilon_2 \neq \varepsilon_3 \neq 0$), plane-strain ($\sigma'_1 \neq \sigma'_2 \neq \sigma'_3$ and $\varepsilon_2 = 0$) and axisymmetric stress state ($\sigma'_1 \neq \sigma'_2 = \sigma'_3$ and $\varepsilon_2 = \varepsilon_3$), respectively. In general loading condition, the geoinclusion-reinforced soil is subjected to a 3D stress state. In other words, under the general loading condition, all the three principal stresses or strains can vary independently. Assuming that the geoinclusion deforms as an ellipse with a uniform tensile stress distribution along its height, the additional confinement can be calculated as [combining Eqs. (1) and (2)]:

(3a) $$\Delta\sigma_2' = -\frac{2M_{\mathrm{m}}}{D_{\mathrm{g}}}\left[\frac{(1-\mu_{\mathrm{g}})k_{\mathrm{c}}+\mu_{\mathrm{g}}}{(1+\mu_{\mathrm{g}})(1-2\mu_{\mathrm{g}})}\right]\varepsilon_2$$

(3b) $$\Delta\sigma_3' = -\frac{2M_{\mathrm{m}}}{D_{\mathrm{g}}}\left[\frac{(1-\mu_{\mathrm{g}})k_{\mathrm{c}}+\mu_{\mathrm{g}}}{(1+\mu_{\mathrm{g}})(1-2\mu_{\mathrm{g}})}\right]\varepsilon_3$$

where ε_2 and ε_3 are the intermediate and minor principal strains in infill (assuming that the geocell and infill soil deform together); k_c is the ratio of circumferential strain to the radial strain.

Eqs. (3a) and (3b) can be employed to calculate the additional confinement provided by cellular geoinclusions under both static and repeated loading conditions. The parameters M_m, D_g, and μ_g are the material properties of geoinclusions and these can be evaluated easily. Moreover, the lateral principal strains (ε_2 and ε_3) in UGM usually comprises recoverable and irrecoverable components that can be calculated using the procedure described in the subsequent sections. The cellular geoinclusion and the infill soil deform together under the applied loading. The irrecoverable component of deformation for the infill soil is primarily attributed to the reorientation or rearrangement of the particles to a denser packing arrangement under loading. The geoinclusion undergoes recoverable deformation until the yield strain of the geoinclusion material is reached. However, the infill deformation usually comprises both recoverable and irrecoverable components due to the elastoplastic nature of granular materials.

Recoverable deformation of infill

The recoverable strains for the static loading case can be determined as follows (Timoshenko and Goodier, 1970):

(4a) $$\varepsilon_2^e = \frac{1}{E}[\sigma_2' - \mu_{\mathrm{s}}(\sigma_1' + \sigma_3')]$$

(4b) $$\varepsilon_3^e = \frac{1}{E}[\sigma_3' - \mu_s(\sigma_1' + \sigma_2')]$$

where ε_2^e and ε_3^e are the recoverable components of intermediate and minor principal strains, respectively; σ'_1, σ'_2 and σ'_3 are the major, intermediate and minor principal stresses; μ_s is the Poisson's ratio of the infill material; E is Young's modulus of the infill material.

Similarly, for the repeated loading condition:

(5a) $$\varepsilon_2^e = \frac{\sigma_{cyc}}{M_R}\left[\frac{\sigma_2' - \mu_s(\sigma_1' + \sigma_3')}{\sigma_1' - \mu_s(\sigma_2' + \sigma_3')}\right]$$

(5b) $$\varepsilon_3^e = \frac{\sigma_{cyc}}{M_R}\left[\frac{\sigma_3' - \mu_s(\sigma_1' + \sigma_2')}{\sigma_1' - \mu_s(\sigma_2' + \sigma_3')}\right]$$

where σ_{cyc} is the cyclic deviator stress; M_R is the resilient modulus of the infill material.

Irrecoverable deformation of infill

The irrecoverable components of intermediate and minor principal strains (ε_2^p, ε_3^p) can be evaluated by using the 3D stress-dilatancy relationship (Schanz and Vermeer 1996). This relationship is given as:

(6) $$\frac{1}{K} = \left(\frac{\sigma_3'}{\sigma_1'}\right)\left(-\frac{d\varepsilon_3^p}{d\varepsilon_1^p}\right) + \left(\frac{\sigma_2'}{\sigma_1'}\right)\left(-\frac{d\varepsilon_2^p}{d\varepsilon_1^p}\right)$$

where $d\varepsilon_1^p$, $d\varepsilon_2^p$, $d\varepsilon_3^p$ are the irrecoverable major, intermediate and minor principal strain rates, respectively; K is the coefficient representing the internal friction [$K = (1+\sin\varphi'_f)/(1-\sin\varphi'_f)$]; and φ'_f is the mobilized friction angle.

On rearranging Eq. (6), $d\varepsilon_2^p$ and $d\varepsilon_3^p$ can be expressed in terms of $d\varepsilon_1^p$ as:

(7a) $$-\frac{d\varepsilon_2^p}{d\varepsilon_1^p} = \frac{(1-R)^{-1}}{b}\cdot\left(1 - D - \frac{R}{K}\right)$$

(7b) $$-\frac{d\varepsilon_3^p}{d\varepsilon_1^p} = \left[1 - \frac{(1-R)^{-1}}{b}\right]\left\{1 - D - \frac{[R^{-1} + b(1-R^{-1})]^{-1}}{K}\right\}$$

where D is the dilatancy rate ($d\varepsilon_v^p/d\varepsilon_1^p$); $d\varepsilon_v^p$ is the volumetric strain rate; R is the stress ratio (σ'_1/σ'_3); b is the intermediate principal stress ratio [$b=(\sigma'_2-\sigma'_3)/(\sigma'_1-\sigma'_3)$].

Thus, ε_2^p and ε_3^p can be calculated by integrating Eqs. (7a) and (7b), respectively.

(8a)
$$\varepsilon_2^p = -\int \frac{(1-R)^{-1}}{b} \cdot \left(1 - D - \frac{R}{K}\right) d\varepsilon_1^p$$

(8b)
$$\varepsilon_3^p = -\int \left[1 - \frac{(1-R)^{-1}}{b}\right] \left\{1 - D - \frac{[R^{-1} + b(1-R^{-1})]^{-1}}{K}\right\} d\varepsilon_1^p$$

Additional confinement

The additional confinement ($\Delta\sigma'_2$ and $\Delta\sigma'_3$) provided by the cellular geoinclusions for static loading condition (loading in vertical direction) can be evaluated by combining Eqs. (3a), (3b), (4a), (4b), (8a) and (8b).

(9a)
$$\Delta\sigma'_2 = -\frac{2M_{\mathrm{m}}}{D_{\mathrm{g}}} \left[\frac{(1-\mu_{\mathrm{g}})k_{\mathrm{c}} + \mu_{\mathrm{g}}}{(1+\mu_{\mathrm{g}})(1-2\mu_{\mathrm{g}})}\right] \left\{\frac{\sigma'_3}{E}[1 - b(1-R) - \mu_{\mathrm{s}}(1+R)] - \int \frac{(1-R)^{-1}}{b}\left[1 - D - \frac{R}{K}\right] d\varepsilon_1^p\right\}$$

(9b)
$$\Delta\sigma'_3 = -\frac{2M_{\mathrm{m}}}{D_{\mathrm{g}}} \left[\frac{(1-\mu_{\mathrm{g}})k_{\mathrm{c}} + \mu_{\mathrm{g}}}{(1+\mu_{\mathrm{g}})(1-2\mu_{\mathrm{g}})}\right] \left\{\frac{\sigma'_3}{E}[1 + \mu_{\mathrm{s}} b(1-R) - \mu_{\mathrm{s}}(1+R)] - \int \left[1 - \frac{(1-R)^{-1}}{b}\right] \left\{1 - D - \frac{[R^{-1} + b(1-R^{-1})]^{-1}}{K}\right\} d\varepsilon_1^p\right\}$$

Thus, for static loading conditions, the additional confinement at a given value of major principal strain (ε_1) can be calculated by using Eqs. (9a) and (9b). However, under repeated/cyclic vertical loading conditions, the strain in UGM also varies with the number of load cycles (Dahlberg 2001). Several models have been developed to predict the behavior of UGM under cyclic loading conditions (Lekarp et al. 2000). In the present study, a power model has been used which incorporates the influence of the stress state and loading conditions on the irrecoverable deformation of UGM (e.g., Puppala et al. 2009).

(10) $$\varepsilon_1{}^{p} = k_1 \cdot \left(\frac{\sigma_{\mathrm{oct}}}{\sigma_{\mathrm{atm}}}\right)^{k_2} \left(\frac{\tau_{\mathrm{oct}}}{\sigma_{\mathrm{atm}}}\right)^{k_3} N^{k_4}$$

where σ_{oct} is the octahedral normal stress; τ_{oct} is the octahedral shear stress; N is the number of load cycles; σ_{atm} is the atmospheric pressure; k_1, k_2, k_3, k_4 are the empirical parameters. The parameter k_1 represents the influence of the infill type on the magnitude of $\varepsilon_1{}^{\mathrm{p}}$ corresponding to the first load cycle. The parameters k_2 and k_3 represent the influence of octahedral normal and shear stresses on the magnitude of $\varepsilon_1{}^{\mathrm{p}}$ corresponding to the first load cycle. The parameter k_4 shows the dependency of $\varepsilon_1{}^{\mathrm{p}}$ on the number of load cycles. It governs the variation of $\varepsilon_1{}^{\mathrm{p}}$ with N.

Differentiating Eq. (10) with respect to N and substituting the value of $d\varepsilon_1{}^{p}$ in Eqs. (8a) and (8b) gives:

(11a) $$\varepsilon_2^{p} = -\int_0^{N_{\mathrm{lim}}} \frac{k_1 k_4 (1-R)^{-1}}{b}\left[1 - D - \frac{R}{K}\right]\left(\frac{\sigma_{\mathrm{oct}}}{\sigma_{\mathrm{atm}}}\right)^{k_2}\left(\frac{\tau_{\mathrm{oct}}}{\sigma_{\mathrm{atm}}}\right)^{k_3} N^{k_4-1}\, dN$$

(11b) $$\varepsilon_3^{p} = -\int_0^{N_{\mathrm{lim}}} k_1 k_4 \left[1 - \frac{(1-R)^{-1}}{b}\right]\left\{1 - D - \frac{[R^{-1} + b(1-R^{-1})]^{-1}}{K}\right\} \times \left(\frac{\sigma_{\mathrm{oct}}}{\sigma_{\mathrm{atm}}}\right)^{k_2}\left(\frac{\tau_{\mathrm{oct}}}{\sigma_{\mathrm{atm}}}\right)^{k_3} N^{k_4-1} dN$$

Similarly, Eqs. (5a) and (5b) can be modified to incorporate the variation of M_{R} with N:

(12a) $$\varepsilon_2^{e} = \int_0^{N_{\mathrm{lim}}} \left\{\sigma_{\mathrm{cyc}}\left[\frac{\sigma_3' + b(\sigma_1' - \sigma_3') - \mu_{\mathrm{s}}(\sigma_1' + \sigma_3')}{\sigma_1' - \mu_{\mathrm{s}} b(\sigma_1' - \sigma_3') - 2\mu_{\mathrm{s}}\sigma_3'}\right]\left(\frac{dM_{\mathrm{R}}^{-1}}{dN}\right)\right\} dN$$

(12b) $$\varepsilon_3^{e} = \int_0^{N_{\mathrm{lim}}} \left\{\sigma_{\mathrm{cyc}}\left[\frac{\sigma_3' - \mu_{\mathrm{s}}(\sigma_1' + \sigma_3') - \mu_{\mathrm{s}} b(\sigma_1' - \sigma_3')}{\sigma_1' - \mu_{\mathrm{s}} b(\sigma_1' - \sigma_3') - 2\mu_{\mathrm{s}}\sigma_3'}\right]\left(\frac{dM_{\mathrm{R}}^{-1}}{dN}\right)\right\} dN$$

Therefore, the additional confinement ($\Delta\sigma'_2$ and $\Delta\sigma'_3$) offered by the geoinclusions for repeated loading condition can be evaluated by combining Eqs. (3a), (3b), (11a), (11b), (12a) and (12b).

$$\Delta\sigma_2' = \int_0^{N_{\mathrm{lim}}} -\frac{2M_{\mathrm{m}}}{D_{\mathrm{g}}}\left[\frac{(1-\mu_{\mathrm{g}})k_{\mathrm{c}}+\mu_{\mathrm{g}}}{(1+\mu_{\mathrm{g}})(1-2\mu_{\mathrm{g}})}\right]\left\{\sigma_{\mathrm{cyc}}\left[\frac{1-b(1-R)-\mu_{\mathrm{s}}(1+R)}{R+\mu_{\mathrm{s}}b(1-R)-2\mu_{\mathrm{s}}}\right]\left(\frac{dM_{\mathrm{R}}^{-1}}{dN}\right) - \frac{k_1k_4\cdot(1-R)^{-1}}{b}\left[1-D-\frac{R}{K}\right]\left(\frac{\sigma_{\mathrm{oct}}}{\sigma_{\mathrm{atm}}}\right)^{k_2}\left(\frac{\tau_{\mathrm{oct}}}{\sigma_{\mathrm{atm}}}\right)^{k_3}N^{k_4-1}\right\}dN \quad (13a)$$

$$\Delta\sigma_3' = \int_0^{N_{\mathrm{lim}}} -\frac{2M_{\mathrm{m}}}{D_{\mathrm{g}}}\left[\frac{(1-\mu_{\mathrm{g}})k_{\mathrm{c}}+\mu_{\mathrm{g}}}{(1+\mu_{\mathrm{g}})(1-2\mu_{\mathrm{g}})}\right]\left\{\sigma_{\mathrm{cyc}}\left[\frac{1+\mu_{\mathrm{s}}b(1-R)-\mu_{\mathrm{s}}(1+R)}{R+\mu_{\mathrm{s}}b(1-R)-2\mu_{\mathrm{s}}}\right]\left(\frac{dM_{\mathrm{R}}^{-1}}{dN}\right) - k_1k_4\left[1-\frac{(1-R)^{-1}}{b}\right]\left\{1-D-\frac{[R^{-1}+b(1-R^{-1})]^{-1}}{K}\right\}\left(\frac{\sigma_{\mathrm{oct}}}{\sigma_{\mathrm{atm}}}\right)^{k_2}\left(\frac{\tau_{\mathrm{oct}}}{\sigma_{\mathrm{atm}}}\right)^{k_3}N^{k_4-1}\right\}dN \quad (13b)$$

Thus, for repeated loading conditions, the extra confinement, offered by geoinclusions after the completion of a given number of load cycles (N_{lim}), can be calculated by using Eqs. (13a) and (13b). The proposed model can also be simplified to cater for the axisymmetric and the plane-strain cases.

Axisymmetric condition

For the axisymmetric condition [$\sigma'_2 = \sigma'_3$ (or $b = 0$), $d\varepsilon_2 = d\varepsilon_3$ and $k_{\mathrm{c}} = 1$], Eq. (7a) is deduced to:

$$R = K(1-D) \quad (14)$$

Upon simplification, Eq. (14) becomes

$$d\varepsilon_3^p = -d\varepsilon_1^p\frac{R}{2\cdot K} \quad (15)$$

Thus, $\Delta\sigma'_3$ for the axisymmetric condition can be given by:

$$\Delta\sigma_3' = \int_0^{N_{\mathrm{lim}}} -\frac{2M_{\mathrm{m}}}{D_{\mathrm{g}}}\left[\frac{1}{(1+\mu_{\mathrm{g}})(1-2\mu_{\mathrm{g}})}\right]\left\{\sigma_{\mathrm{cyc}}\left[\frac{1-\mu_{\mathrm{s}}(1+R)}{R-2\mu_{\mathrm{s}}}\right]\left(\frac{dM_{\mathrm{R}}^{-1}}{dN}\right) - \frac{k_1k_4R}{2K}\left(\frac{\sigma_{\mathrm{oct}}}{\sigma_{\mathrm{atm}}}\right)^{k_2}\left(\frac{\tau_{\mathrm{oct}}}{\sigma_{\mathrm{atm}}}\right)^{k_3}N^{k_4-1}\right\}dN \quad (16)$$

Plane-strain condition

For the plane-strain condition ($d\varepsilon_2 = 0$), Eq. (7a) can be simplified as:

$$d\varepsilon_3^p = -d\varepsilon_1^p \frac{R}{K} \tag{17}$$

The $\Delta\sigma'_3$ for the plane-strain condition can thus be expressed as:

$$\Delta\sigma_3' = \int_0^{N_{\text{lim}}} -\frac{2M_{\text{m}}}{D_{\text{g}}}\left[\frac{(1-\mu_{\text{g}})k_{\text{c}}+\mu_{\text{g}}}{(1+\mu_{\text{g}})(1-2\mu_{\text{g}})}\right]\left\{\sigma_{\text{cyc}}\left[\frac{(1-\mu_{\text{s}})-\mu_{\text{s}}R}{R(1-\mu_{\text{s}})-\mu_{\text{s}}}\right]\left(\frac{dM_{\text{R}}^{-1}}{dN}\right) - \frac{k_1k_4R}{K}\left(\frac{\sigma_{\text{oct}}}{\sigma_{\text{atm}}}\right)^{k_2}\left(\frac{\tau_{\text{oct}}}{\sigma_{\text{atm}}}\right)^{k_3}N^{k_4-1}\right\}dN \tag{18}$$

IDENTIFICATION OF MODEL PARAMETERS

The present model comprises the following parameters: M_{m}, D_{g}, μ_{g}, b, M_{R}, E, μ_{s}, k_1, k_2, k_3, k_4, φ'_{f}, and D. The first three parameters are the geoinclusion properties. The parameter b depends on the external loading conditions. The parameters M_{R}, E and μ_{s} for a particular cellular geoinclusion reinforced UGM can be determined from conventional laboratory experiments. The empirical parameters k_1, k_2, k_3 and k_4 can be determined by fitting the experimental curves of irrecoverable vertical strain with the number of load cycles (N) for reinforced UGM at different loading conditions. Furthermore, parameters φ'_{f} and D can be determined by conducting true-triaxial tests ($\sigma'_1 \neq \sigma'_2 \neq \sigma'_3$) on geoinclusion reinforced UGM. Moreover, φ'_{f} and D depend on the parameter b (Wang and Lade 2001). However, a unique relationship between these parameters is not yet established. Therefore, the values of b, φ'_{f} and D are varied to investigate their influence on the additional confinement.

RESULTS AND DISCUSSION

Using the present approach, the influence of infill properties, stress levels and geoinclusion type on additional confinement are investigated. Table 1 lists the parameters used in the analysis. The results are expressed in terms of normalized additional confinement ($k_{\sigma,2}$ =

$\Delta\sigma'_2/\sigma'_2$ and $k_{\sigma,3} = \Delta\sigma'_3/\sigma'_3$) and additional confinement ratio (ACR). The ACR is the ratio of extra confinement offered by the geoinclusions in lateral orthogonal directions (i.e., $\Delta\sigma'_2/\Delta\sigma'_3$). These normalized ratios are used to present the results in a concise form. Moreover, the use of ACR allows an efficient comparison of $\Delta\sigma'_2$ with $\Delta\sigma'_3$. The value of ACR ranges between 0 and 1 corresponding to the cases when $\Delta\sigma'_2 = 0$ and $\Delta\sigma'_2 = \Delta\sigma'_3$, respectively.

Influence of infill properties and stress levels

Fig. 3a shows the variation of ACR with the mobilized friction angle (φ'_f) and dilatancy rate (D). It can be observed that ACR increases with a decrease in D (e.g. 370% increment when D decreases from -1 to -0.2, for $\varphi'_f = 40°$). Moreover, it decreases with an increase in φ'_f for a particular value of D (e.g. 98% reduction when φ'_f increases from 40° to 60° for $D = -0.2$). This variation is probably due to a reduction in ε_2 with an increase in D and K [refer to Eq. (8a)]. Consequently, a smaller magnitude of confinement ($\Delta\sigma'_2$) is mobilized in the direction of σ'_2 for higher values of D and K. Thus, a weak infill (exhibited by small φ'_f) with a smaller D may mobilize more confinement, $\Delta\sigma'_2$, than a strong infill with a greater D (for a particular value of b). On the contrary, ε_3 increases with an increase in D and K [refer to Eq. (8b)]. This increases the magnitude of $\Delta\sigma'_3$. Therefore, an optimum value of φ'_f and D may be required to derive maximum benefits from geoinclusion reinforcement.

Nevertheless, this variation also depends on stress levels. Fig. 3b shows the influence of parameter b on ACR. It is observed that ACR decreases with an increase in b (e.g. 92% reduction when b increases from 0.1 to 0.3 for $D = -0.2$). This is because ε_2 reduces with an increase in b. As a consequence, the extra confinement $\Delta\sigma'_2$ undergoes substantial reduction. Thus, σ'_2 significantly influences the magnitude of extra confinement offered by the geoinclusion.

It can be noted that parameter b at the plane-strain condition (b_{ps}) for the above case is 0.32. Therefore, the magnitude of ACR is nearly equal to 0 for b = 0.3. Moreover, ACR becomes 0 for $b \geq b_{ps}$ because ε_2 becomes compressive if b exceeds b_{ps}. Due to lack of experimental/field data, it is very difficult at this stage to visualize the deformation behavior of geoinclusion once b exceeds b_{ps}. Therefore, b has been normalized with b_{ps} in subsequent section to show its influence on additional confinement. Fig. 3c shows the polar contour plot of ACR for σ'_3 = 15 kPa and D = -0.2 to elucidate the influence of φ'_f and b/b_{ps} ratio on ACR. The radial and polar coordinates in the plot correspond to the values of parameters k_c and b/b_{ps} ratio respectively. The four different sectors in the plot represent the ACR values for $\varphi'_f = 40^\circ$, 45°, 50° and 55°. The radial boundary of each sector is marked by the plane-strain (b/b_{ps} = 1) and the axisymmetric conditions (b/b_{ps} = 0). It can be observed that ACR decreases with an increase in b/b_{ps} and φ'_f. This may be attributed to the reduction in the magnitude of ε_2 with an increase in φ'_f and b/b_{ps}.

Influence of geoinclusion type

The geoinclusion type may influence the magnitude of additional confinement. Therefore, five different types of geoinclusion materials, namely, HDPE, woven coir fiber geotextile, nonwoven polypropylene fiber geotextile, rubber membrane (with three different thicknesses) and rubber tire, have been used in the analysis. Fig. 4a shows the load vs. strain curves of the five materials obtained from tension tests (Henkel and Gilbert 1952; Koerner 2012; Biabani 2015; Indraratna et al. 2017; Lal et al. 2017). It can be observed that each material exhibits distinct load-strain response. HDPE shows an elastic-perfectly plastic response with high initial modulus, while nonwoven geotextile shows a strain hardening response with progressively increasing modulus. The secant modulus of coir geotextile is initially intermediate to that of HDPE and polypropylene geotextile. However, after 12.5% strain, the secant modulus of coir geotextile exceeds the modulus of HDPE. Furthermore, the rubber tire and rubber membranes have the maximum and minimum modulus among all the materials, respectively.

Fig. 4b shows the variation of normalized additional confinement with N for the five different geoinclusion materials at σ'_3 = 15 kPa, b = 0.1, D = -0.2 and $\varphi'_f = 50^{\circ}$. It can be observed that the rubber tire provides the maximum confinement to the infill in the direction of σ'_3. This is reasonable since the modulus of rubber tire is the maximum among the five materials at a particular magnitude of strain. HDPE provides a higher confinement than coir geotextile, polypropylene geotextile and rubber membranes. However, if the mobilized strain increases beyond 12.5%, the magnitude of confinement provided by coir geotextile may exceed that provided by HDPE [refer to Fig. 4a]. Nevertheless, the mobilized strain, in this case, is below 12.5%. Consequently, HDPE provides a higher confinement than coir geotextile throughout the loading schedule. The extra confinement offered by polypropylene geotextile and rubber membranes is very small as compared to rubber tire, HDPE and woven coir geotextile due to their low secant modulus.

Similar behavior is observed in the direction of σ'_2. The magnitude of $k_{\sigma,2}$ is the highest for rubber tire followed by HDPE, coir geotextile, polypropylene geotextile and rubber membranes. However, $k_{\sigma,2}$ is smaller than $k_{\sigma,3}$ for all the materials. This is due to the mobilization of a small magnitude of strain in the direction of σ'_2.

Hence, the additional confinement provided by the geoinclusion significantly depends on the type of the constituent material. Usually, the confinement increases with an increase in geoinclusion modulus. However, the selection of an appropriate geoinclusion must be based on its intended function and scope of the project. Moreover, the additional confinement ($\Delta\sigma'_2$ and $\Delta\sigma'_3$) is not only directionally sensitive, but also sensitive to parametric variations. Therefore, simplification of 3D into 2D (axisymmetric or plane-strain) stress state may result into either over-predictive or conservative estimates. Thus, the present model yields more accurate results as compared to the existing models.

In practice, the geoinclusion-stabilized soil is more likely to be subjected to a complex 3D stress state. The present model evaluates the extra confinement offered by the cellular geoinclusions in the directions of σ'_2 and σ'_3. Moreover, it can capture the variations in the confinement mobilized in the two orthogonal directions due to changes in stress levels, infill and geoinclusion properties. Thus, the model can also help in the selection of adequate material parameters for deriving maximum potential benefits from geoinclusion reinforcement.

MODEL VALIDATION

Limited laboratory or field data are available on the magnitude of additional confinement provided by the cellular geoinclusions in the 3D ($\sigma'_1 \neq \sigma'_2 \neq \sigma'_3$) loading conditions. Nevertheless, the present model is validated against the results of the static triaxial tests on geocell-reinforced soils conducted by Bathurst and Rajagopal (1993) and Rajagopal et al. (1999), and the repeated load triaxial tests conducted by Mengelt et al. (2006). Table 2 lists the input parameters used in the predictions. Fig. 5a compares the additional confinement calculated using the present model with the experimental data. It is observed that the predicted values vary by 1% to 20% from the experimental results.

The model is also used to predict the extra confinement offered by geocells for the plane-strain repeated load tests, conducted by Indraratna et al. (2015). The values of the parameters used in the prediction are listed in Table 2. Fig. 5b compares the predicted and experimentally observed results. The results are expressed in terms of normalized additional confinement ($k_{\sigma,3}$). The predicted results are in a good agreement with the experimental data. A slight deviation from the experimental data can occur if the value of modulus is arbitrarily selected. In fact, the modulus needs careful evaluation by conducting the tensile tests or junction peel tests. This is because, it depends on the type of test arrangement (i.e. specimen with or without welds) and the nature of the test (i.e. wide width, junction peel, split). Nevertheless, it is apparent that the present approach can provide reliable estimates of the extra confinement, offered by geoinclusions.

CONCLUSIONS

A semi-empirical model has been developed to evaluate the extra confinement offered by the cellular geoinclusions under the 3D stress state ($\sigma'_1 \neq \sigma'_2 \neq \sigma'_3$). The results indicate that the magnitude of additional confinement is sensitive to the stress state (axisymmetric, plane-strain and 3D), type of inclusion and the parametric variations. The additional confinement ratio (ACR) varies between 0 and 1 for the 3D stress state, which indicates that the simplification of the 3D stress state to plane-strain or axisymmetric stress states yields conservative or over-predicted results, respectively. Moreover, in comparison to $\Delta\sigma'_3$, the additional confinement in the direction of σ'_2 ($\Delta\sigma'_2$) decreases with an increase in dilatancy rate (D), mobilized friction angle (φ'_f) and the intermediate principal stress ratio (b). Furthermore, the magnitude of extra confinement increases with an increase in geoinclusion modulus. Thus, the present model provides a realistic assessment of additional confinement for deriving maximum potential benefits from geoinclusion reinforcement with a convenient selection of adequate material parameters.

ACKNOWLEDGEMENTS

This research is supported by an Australian Government Research Training Program Scholarship. The authors wish to thank the anonymous reviewers for their valuable comments and suggestions.

REFERENCES

Bathurst, R.J., and Knight, M.A. 1998. Analysis of geocell reinforced soil covers over large span conduits. Computers and Geotechnics, **22**(3-4): 205–219.

Bathurst, R.J., and Rajagopal, K. 1993. Large-scale triaxial compression testing of geocell-reinforced granular soils. Geotechnical Testing Journal, **16**(3): 296–303.

Biabani, M.M. 2015. Behaviour of geocell-reinforced subballast under cyclic loading in plane strain condition. Ph.D. thesis, Faculty of Engineering and Information Sciences, University of Wollongong, Wollongong, Australia.

Dahlberg, T. 2001. Some railroad settlement models–a critical review. Proceedings of the Institution of Mechanical Engineers, Part F: Journal of Rail and Rapid Transit, **215**(4): 289–300.

Forsyth, R.A., and Egan, J.P. 1976. Use of waste materials in embankment construction. Transportation Research Record, **593**: 3–8.

Garga, V.K., and O'shaughnessy, V. 2000. Tire-reinforced earthfill. Part 1: Construction of a test fill, performance, and retaining wall design. Canadian Geotechnical Journal, **37**(1): 75–96.

Han, J., Yang, X., Leshchinsky, D., and Parsons, R. 2008. Behavior of geocell-reinforced sand under a vertical load. Transportation Research Record: Journal of the Transportation Research Board, **2045**:95-101.

Henkel, D., and Gilbert, G. 1952. The effect measured of the rubber membrane on the triaxial compression strength of clay samples. Géotechnique, **3**(1): 20–29.

Indraratna, B., Biabani, M.M., and Nimbalkar, S. 2015. Behavior of geocell-reinforced subballast subjected to cyclic loading in plane-strain condition. Journal of Geotechnical and Geoenvironmental Engineering, **141**(1). doi: 10.1061/(ASCE)GT.1943-5606.0001199.

Indraratna, B., Sun, Q., and Grant, J. 2017. Behaviour of subballast reinforced with used tyre and potential application in rail tracks. Transportation Geotechnics, **12**: 26–36.

Koerner, R.M. 2012. Designing with geosynthetics (sixth edition). Xlibris Corporation, Bloomington, USA.

Lal, D., Sankar, N., and Chandrakaran, S. 2017. Effect of reinforcement form on the behaviour of coir geotextile reinforced sand beds. Soils and Foundations, **57**(2): 227–236.

Lekarp, F., Isacsson, U., and Dawson, A. 2000. State of the art. II: Permanent strain response of unbound aggregates. Journal of Transportation Engineering, **126**(1): 76–83. doi: 10.1061/(ASCE)0733-947X(2000)126:1(76).

Leshchinsky, B., and Ling, H.I. 2013a. Effects of geocell confinement on strength and deformation behavior of gravel. Journal of Geotechnical and Geoenvironmental Engineering, **139**(2): 340–352. doi: 10.1061/(ASCE)GT.1943-5606.0000757.

Leshchinsky, B., and Ling, H.I. 2013b. Numerical modeling of behavior of railway ballasted structure with geocell confinement. Geotextiles and Geomembranes, **36**: 33–43.

Liu, Y., Deng, A., and Jaksa, M. 2018. Three-dimensional modeling of geocell-reinforced straight and curved ballast embankments. Computers and Geotechnics, **102**: 53–65.

Mengelt, M., Edil, T.B., and Benson, C.H. 2006. Resilient modulus and plastic deformation of soil confined in a geocell. Geosynthetics International, **13**(5): 195–205.

Nimbalkar, S., Punetha, P., and Kaewunruen, S. 2019. Performance improvement of ballasted railway tracks using geocells: present state of the art. *In* Handbook of Geocells. *Edited by* T.G. Sitharam, A. Hegde and S. Kolathayar. Springer. (In press)

Puppala, A.J., Saride, S., and Chomtid, S. 2009. Experimental and modeling studies of permanent strains of subgrade soils. Journal of Geotechnical and Geoenvironmental engineering, **135**(10): 1379–1389. doi: 10.1061/(ASCE)GT.1943-5606.0000163.

Rajagopal, K., Krishnaswamy, N.R., and Latha, G.M. 1999. Behaviour of sand confined with single and multiple geocells. Geotextiles and Geomembranes, **17**(3): 171–184.

Raymond, G.P. 2001. Failure and reconstruction of a gantry crane ballasted track. Canadian Geotechnical Journal, **38**(3): 507–529.

Satyal, S.R., Leshchinsky, B., Han, J., and Neupane, M. 2018. Use of cellular confinement for improved railway performance on soft subgrades. Geotextiles and Geomembranes, **46**(2): 190–205.

Schanz, T., and Vermeer, P.A. 1996. Angles of friction and dilatancy of sand. Géotechnique, **46**(1): 145–152.

Selig, E.T., and Waters, J.M. 1994. Track geotechnology and substructure management, Thomas Telford, London.

Sun, Y., Nimbalkar, S., and Chen, C. 2018. Grading and frequency dependence of the resilient modulus of ballast. Géotechnique Letters. (In press).

Timoshenko, S.P., and Goodier, J.N. 1970. Theory of elasticity, McGraw Hill, New York.

Wang, Q., and Lade, P.V. 2001. Shear banding in true triaxial tests and its effect on failure in sand. Journal of Engineering Mechanics, **127**(8): 754–761.

Yang, X., and Han, J. 2013. Analytical model for resilient modulus and permanent deformation of geosynthetic-reinforced unbound granular material. Journal of Geotechnical and Geoenvironmental Engineering, **139**(9): 1443–1453. doi: 10.1061/(ASCE)GT.1943-5606.0000879.

Zhou, H. and Wen, X. 2008. Model studies on geogrid-or geocell-reinforced sand cushion on soft soil. Geotextiles and Geomembranes, **26**(3): 231–238.

Table captions

Table 1. Input parameters for the parametric study.

Table 2. Parameters for predicting the additional confinement under the plane-strain and axisymmetric conditions.

Table 1. Input parameters for the parametric study.

Parameter	Value
Test type	Repeated load test
Loading condition	General
Geoinclusion material	HDPE (unless otherwise stated)
Infill material	Subballast
Frequency (Hz)	10
D_g (m)	0.24, 0.54 (for rubber tire)
σ'_1 (kPa)	160
σ'_3 (kPa)	15, 20, 25, 30
σ_{cyc} (kPa)	145, 140, 135, 130
σ_{atm} (kPa)	101.325
N_{lim}	500 000
μ_g	0.3
μ_s	0.35
D^*	-0.2, -0.4, -0.6, -0.8, -1.0
k_1	19.12
k_2	-3
k_3	8.42
k_4	0.129
φ'_f (°)	40, 45, 50, 55, 60

* Negative sign is assigned for dilative behavior

Table 2. Parameters for predicting the additional confinement under the plane-strain and axisymmetric conditions.

Parameter	Axisymmetric			Plane-strain
	Bathurst and Rajagopal (1993)	Rajagopal et al. (1999)	Mengelt et al. (2006)	Indraratna et al. (2015)
Infill material	Dense SS	Sand	Sand	Subballast
Geocell material	Polyethylene	PP-W, PP-NW	HDPE	HDPE
Frequency (Hz)	Not applicable	Not applicable	1	10–30
D_g (m)	0.2	0.1	0.25	0.24
σ'_1 (kPa)	1 050	550–860	25–100	166
σ'_3 (kPa)	25	100	1	5–30
N_{lim}	Not applicable	Not applicable	1 500	500 000
φ'_f (°)	72.5	44.1–52.4	67.4–78.6	Varies with N
E (MPa)	46.2	21.9–38.2	Not applicable	Not applicable
M_R (MPa)	Not applicable	Not applicable	16–41	Varies with N
μ_g	0.30	0.30	0.30	0.30
μ_s	0.35	0.35	0.35	0.35
k_c	1	1	1	0.075
k_1	Not applicable	Not applicable	Not applicable	19.12–72.17
k_2	Not applicable	Not applicable	Not applicable	-3
k_3	Not applicable	Not applicable	Not applicable	8.42
k_4	Not applicable	Not applicable	Not applicable	0.129–0.156
σ_{atm} (kPa)	101.325	101.325	101.325	101.325

Note: Geocell modulus is the secant modulus corresponding to the magnitude of mobilized strain; SS = silica sand; PP-W = polypropylene woven geotextile; PP-NW = polypropylene nonwoven geotextile; HDPE = high-density polyethylene.

Figure captions

Fig. 1. The behavior of railway embankment under train traffic-induced loads: (a) without cellular geoinclusion; (b) with cellular geoinclusion

Fig. 2. Deformation of cellular geoinclusion under different stress states: **(a)** general; **(b)** plane-strain; **(c)** axisymmetric

Fig. 3. Variation of additional confinement ratio (ACR) with **(a)** mobilized friction angle (φ'_f) and dilatancy rate (D); **(b)** dilatancy rate (D) for b = 0.1, 0.2 and 0.3; **(c)** b/b_{ps} ratio and φ'_f

Fig. 4(a). Tensile load-strain curves for five different types of cellular geoinclusion materials; **(b).** variation of normalized additional confinement ($k_{\sigma,2}$ and $k_{\sigma,3}$) with the number of load cycles (N)

Fig. 5. Comparison of the additional confinement computed using the present model with the experimental data under **(a)** axisymmetric condition; **(b)** plane-strain condition

Fig. A1. Stress profile of 3D cellular geoinclusion under general stress state

APPENDIX

The Fig. A1 shows the stress profile of the 3D cellular geoinclusion under general stress state. Taking equilibrium of forces along the directions 2 and 3 gives:

(A1) $$(\sigma_2' + \Delta\sigma_2')D_g - \sigma_2' D_g - 2\sigma_{c,2} t_g = 0$$

(A2) $$(\sigma_3' + \Delta\sigma_3')D_g - \sigma_3' D_g - 2\sigma_{c,3} t_g = 0$$

where $\Delta\sigma'_2$ and $\Delta\sigma'_3$ are the additional confining pressures in the direction of intermediate (σ'_2) and minor principal stresses (σ'_3), respectively; $\sigma_{c,2}$ and $\sigma_{c,3}$ are the circumferential stresses in the direction of σ'_2 and σ'_3, respectively; D_g and t_g are diameter and thickness of geoinclusion, respectively.

On simplification, $\Delta\sigma'_2$ and $\Delta\sigma'_3$ can be expressed as:

(A3) $$\Delta\sigma_2' = \frac{2\sigma_{c,2} t_g}{D_g}$$

(A4) $$\Delta\sigma_3' = \frac{2\sigma_{c,3} t_g}{D_g}$$

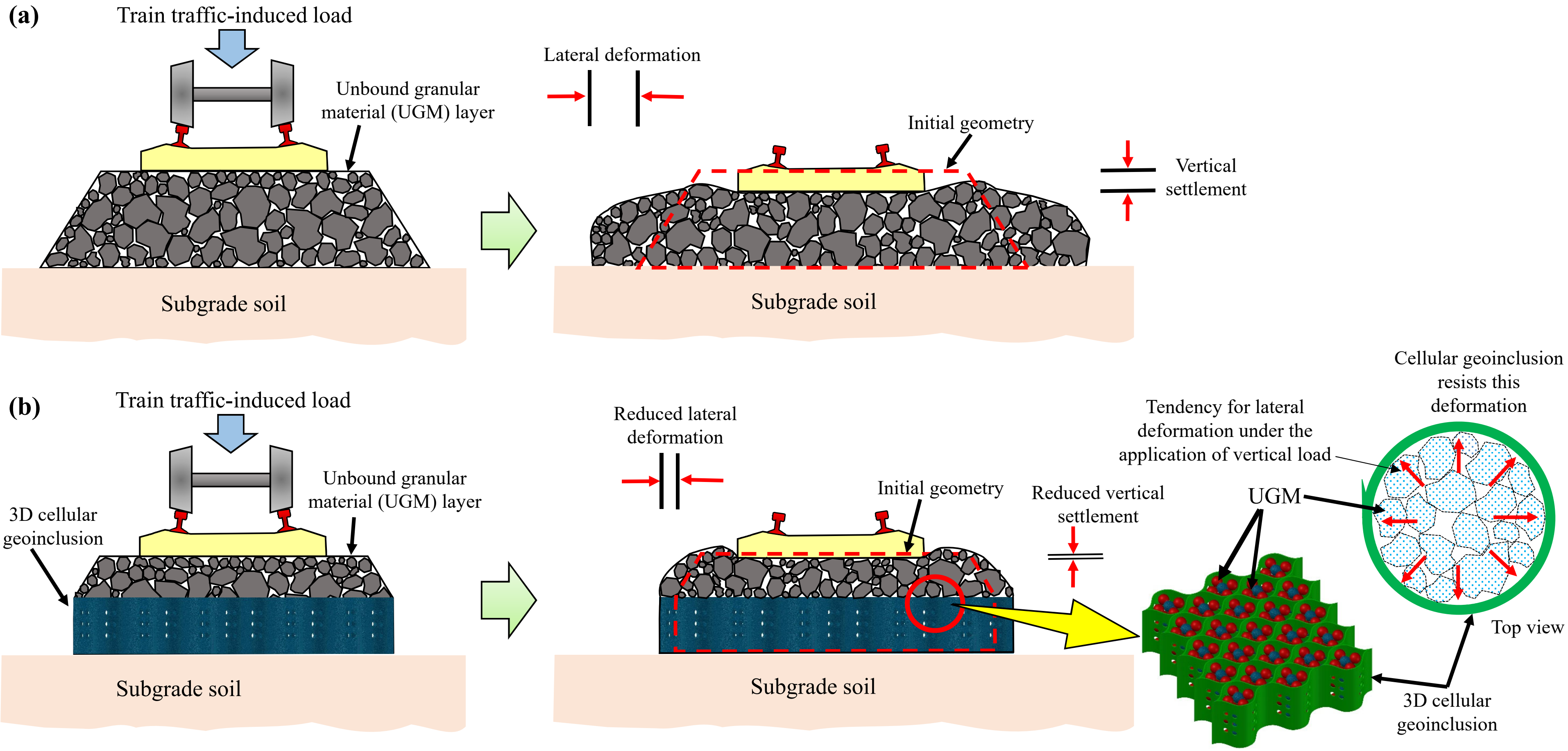

Fig. 1 The behaviour of railway embankment under train traffic-induced loads: (a) without cellular geoinclusion; (b) with cellular geoinclusion

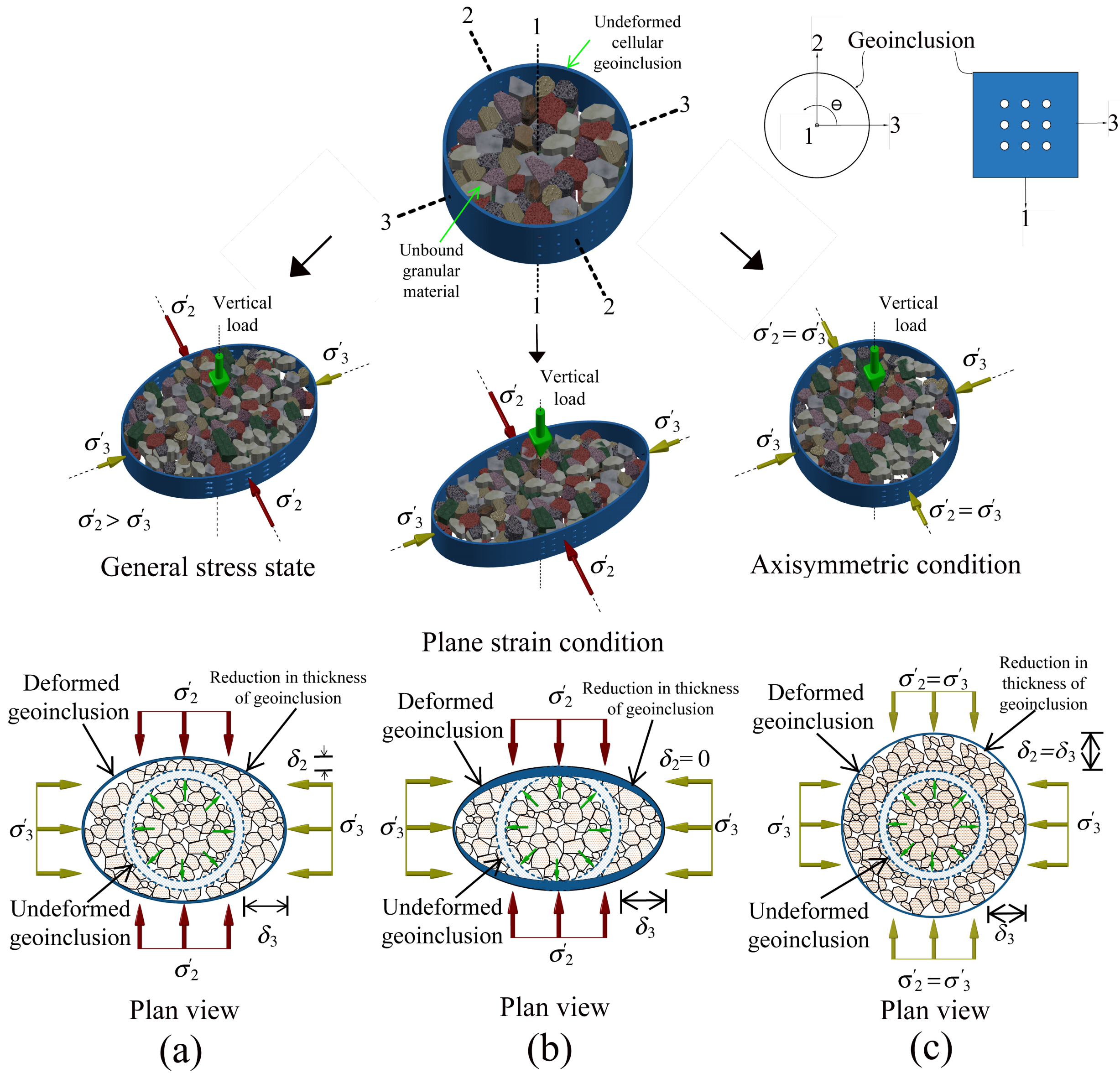

Fig. 2. Deformation of cellular geoinclusion under different stress states: (a) general; (b) plane-strain; (c) axisymmetric

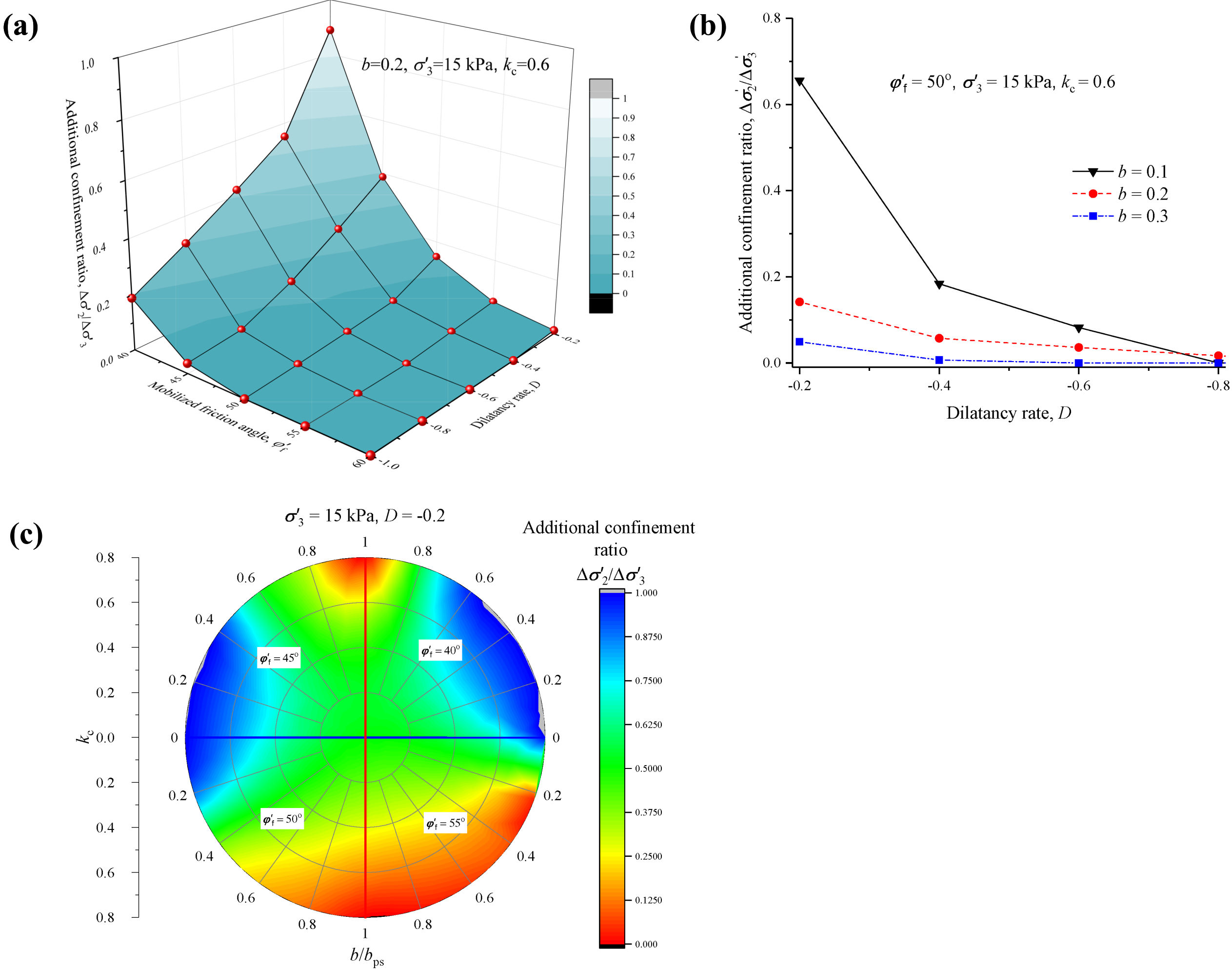

Fig. 3 Variation of additional confinement ratio (ACR) with (a) mobilized friction angle (φ'_{f}) and dilatancy rate (D); (b) dilatancy rate (D) for b = 0.1, 0.2 and 0.3; (c) b/b_{ps} ratio and φ'_{f}

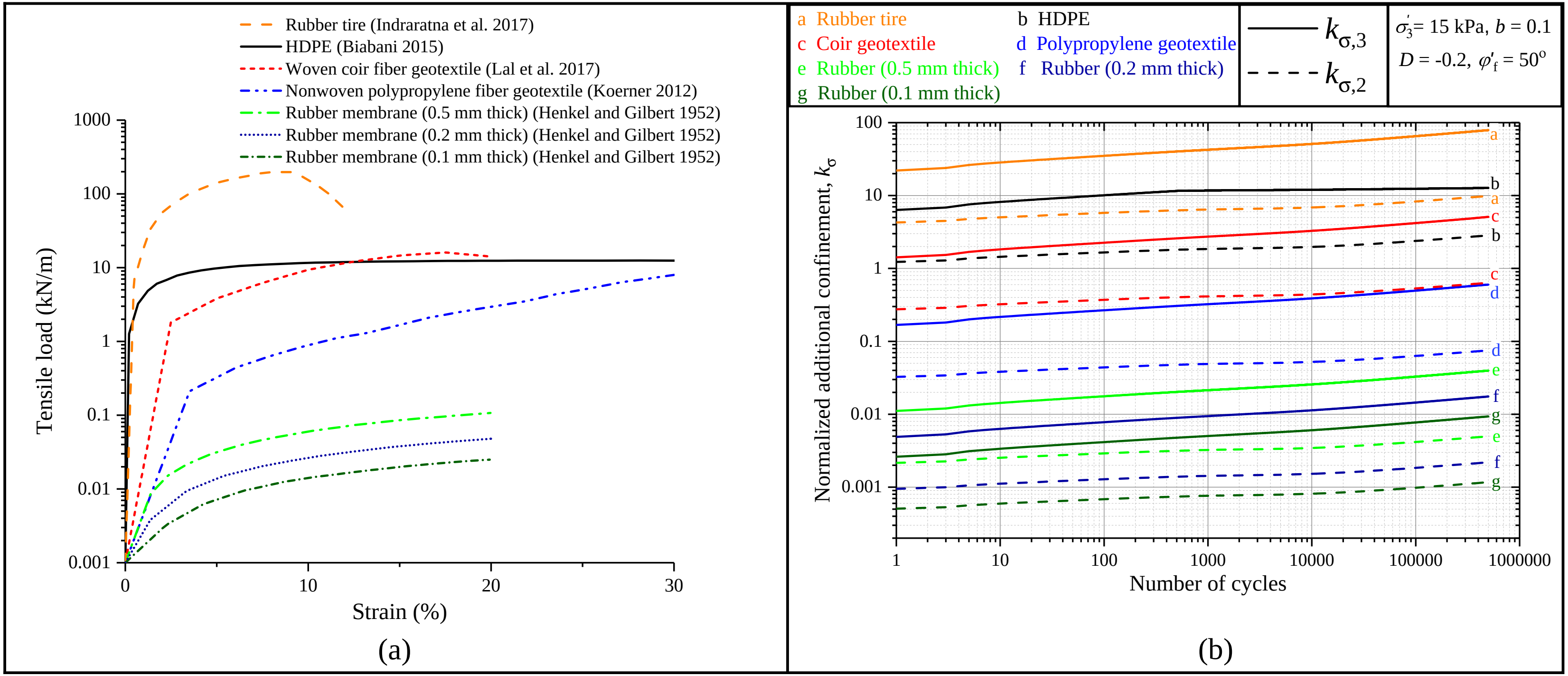

Fig. 4(a). Tensile load-strain curves for five different types of cellular geoinclusion materials; **(b).** variation of normalized additional confinement ($k_{\sigma,2}$ and $k_{\sigma,3}$) with the number of load cycles (N)

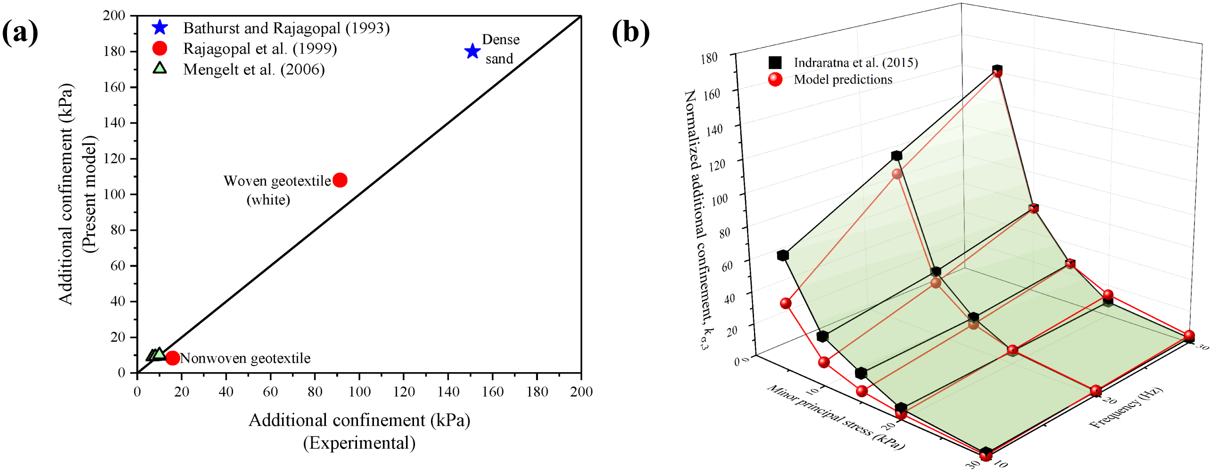

Fig. 5 Comparison of the additional confinement computed using the present model with the experimental data under (a) axisymmetric condition; (b) plane-strain condition

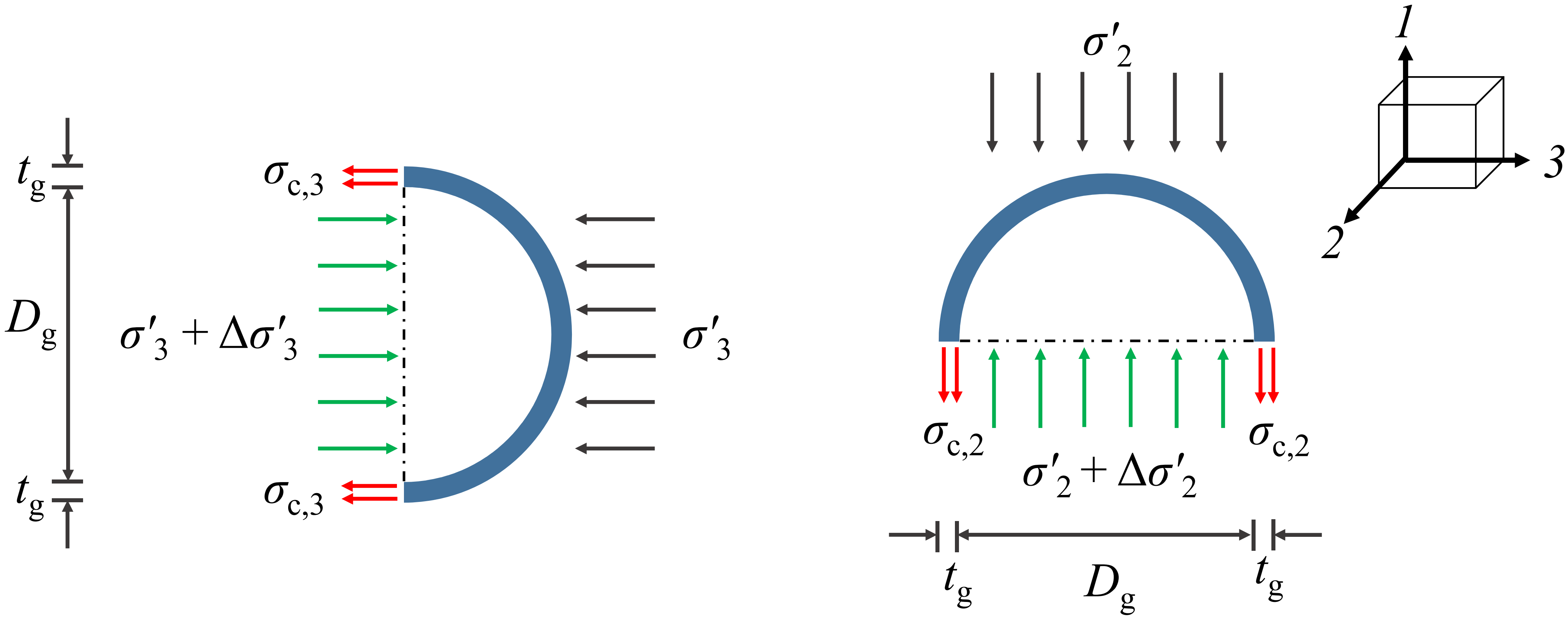

Taking equilibrium of forces along direction 3:

$$(\sigma'_3 + \Delta\sigma'_3) \cdot D_g = \sigma'_3 \cdot D_g + 2 \cdot \sigma_{c,3} \cdot t_g$$

$$\Delta\sigma'_3 = (2 \cdot \sigma_{c,3} \cdot t_g)/D_g$$

Taking equilibrium of forces along direction 2:

$$(\sigma'_2 + \Delta\sigma'_2) \cdot D_g = \sigma'_2 \cdot D_g + 2 \cdot \sigma_{c,2} \cdot t_g$$

$$\Delta\sigma'_2 = (2 \cdot \sigma_{c,2} \cdot t_g)/D_g$$

Fig. A1 Stress profile of 3D cellular geoinclusion under general stress state